Physics of wurtzite ferroelectrics

Hiroki Moriwake, Betul Akkopru-Akgun, Sebastian Calderon, Elizabeth C. Dickey,* and Prashun Gorai*

Ferroelectricity was long considered incompatible with the wurtzite structure, but the recent discovery of switchable polarization in wurtzite alloys has renewed interest in these materials for integrated electronic and memory applications. The development of wurtzite ferroelectrics faces significant technological challenges, which can be addressed through a fundamental physical understanding of their dielectric and ferroelectric properties. This article focuses on the physics that govern the polarization switching behavior, emphasizing the atomic- and meso-scale (domain) mechanisms involved in the transition between polarization states. A distinguishing feature of this article is a deep dive into the role of intrinsic and extrinsic defects—an area that has received limited attention in prior reviews, but is increasingly recognized as central to polarization switching, coercive fields, leakage, and fatigue. We highlight how defect behavior evolves during processing and electrical cycling, often contributing to long-term degradation. We also introduce powerful first-principles defect calculations, common in semiconductors but not yet widespread in ferroelectrics, as tools to understand and design materials. By integrating recent theoretical and experimental insights, we aim to provide a framework for advancing wurtzite ferroelectrics.

Introduction

Ferroelectric materials are polar non-centrosymmertric crystal structures having an electric polarization that can be switched between crystallographically degenerate states with the application of an electric field. The wurtzite structure (S.G.: $P6_3mc$) is a polar crystal structure as shown in **Figure 1**, but it has long been regarded to be non-ferroelectric (nonswitchable) because of the large atomic displacements and bond breaking necessary to transition from one polarization state to the other, especially in crystals with a high degree of polar covalent bonding. Here and subsequently, the term "wurtzite" also includes wurtzite-derived structures, including wurtzite-type solid solutions such as $Al_{1-x}Sc_xN$.[1]

Spontaneous polarization in wurtzite structures

Unlike perovskites, an initial challenge in wurtzites was to identify the correct nonpolar reference phase, which is intimately related to the magnitude of the spontaneous polarization (P_s) and switching mechanism. Prior to the discovery of ferroelectricity, modeling and predicting P_s in wurtzite materials was largely motivated by the need to understand polarization discontinuities at interfaces.[2] The sign and magnitude of P_s, however, depend upon the reference structure, according to the modern theory of polarization.[3–5] With the discovery of ferroelectricity in wurtzites, it became apparent that different reference structures were being utilized in the literature, each giving a different value and sign for P_s.[6] The early attempts at theoretically estimating P_s in wurtzite materials from Bernardini et al., using zincblende as the reference state, resulted in underestimated P_s[7] compared to the ones calculated by Dreyer et al. using a layered hexagonal structure.[6] Fichtner et al., using the modern theory of polarization, clarified the layered hexagonal BN-like (hBN-like) structure as the appropriate reference non-polar structure, as shown in Figure 1a.[8] Using this reference structure, the N-polar and metal(M)-polar phases of wurtzite MN exhibit P_s vectors pointing downward (Figure 1b) and upward (Figure 1c), respectively. Utilizing this reference frame, the sign and magnitude of P_s can be calculated from the structural parameters and the Born effective charges (Z^*) using Equation 1, which has been successfully applied to perovskite ferroelectrics.[9,10]

$$\Delta P_\beta = \frac{e}{\Omega}\sum_s Z^*_{s,\alpha\beta}\Delta\vec{r}_{s,\alpha}, \quad (1)$$

Hiroki Moriwake, Nanostructures Research Laboratory, Japan Fine Ceramics Center, Nagoya 456-8587, Japan; MDX Research Center for Element Strategy, Institute of Science Tokyo, Yokohama 226-8503, Japan; moriwake@jfcc.or.jp
Betul Akkopru-Akgun, Materials Science and Engineering, The Pennsylvania State University, University Park, USA; bua134@psu.edu
Sebastian Calderon, Materials Science and Engineering, Carnegie Mellon University, Pittsburgh, USA; scaldero@andrew.cmu.edu
Elizabeth C. Dickey, Materials Science and Engineering, Carnegie Mellon University, Pittsburgh, USA; ecdickey@cmu.edu
Prashun Gorai, Chemical and Biological Engineering, Rensselaer Polytechnic Institute, Troy, USA; goraip@rpi.edu
*Corresponding author
doi:10.1557/s43577-025-00972-1

© The Author(s) 2025

where Δr is the displacement from the reference centrosymmetric reference structure, e is the electronic charge, and Ω is the unit cell volume. In the wurtzite structure, P_s is constrained along the $\langle 0001 \rangle$ c-axis and this reduces to:

$$P_s = \frac{2e}{\Omega} Z^*_{ion} \Delta \vec{r}_{ion}. \quad (2)$$

Taking wurtzite ZnO as an example, with a cell volume of 49.72 Å^3, a Born effective charge of 2.163 for Zn and an average Zn displacement of 0.638 Å from the centrosymmetric structure, the resulting P_s is 0.888 C/m^2.[11] The direction of P_s results from the displacement vector, positive (up) for metal-polar direction and negative (down) for oxygen-polar configuration, similar to wurtzite *M*N shown in Figure 1.

With this approach, P_s can be experimentally determined by analyzing atomic positions within the structure (e.g., by structure refinement via scattering experiments or through atomic-resolution transmission electron microscopy techniques), which is more applicable to thin films. This structure-based method has been applied to a compositional series of $Al_{1-x}B_xN$ thin films,[12] enabling the calculation of P_s even at the highest boron concentrations, where conventional polarization–electric field (P–E) loop measurements are hindered by significant leakage currents. The results reveal a strong correlation between P_s and the crystalline quality of the films, as boron content increases, crystallinity deteriorates, leading to a corresponding reduction in P_s.

The ability to probe polarization at the local scale opens new possibilities for investigating P_s at interfaces and defective regions, down to the unit-cell level. Electron microscopy-based calculations have demonstrated that with appropriate experimental configuration and careful sample preparation, polarization measurements in these structures can achieve accuracy within 5–15 percent.[13] Ultimately, such structure-based measurements of the spontaneous polarization should correlate with the remanent polarization measured in ferroelectric hysteresis loops. When inferring P_s via the displacement currents induced by ferroelectric switching, however, it is important to recognize other potential contributions to the measured current, including electrical leakage and contributions from piezoelectric displacement currents.

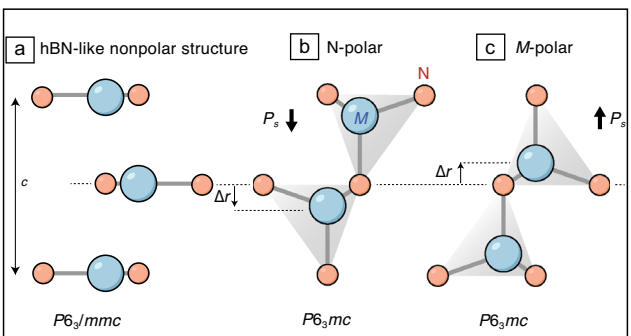

Figure 1. (a) Reference hexagonal BN-like non-polar structure (S.G.: $P6_3/mmc$) of wurtzite metal-nitride (*M*N). The spontaneous polarization (P_S) points downward for N-polar wurtzite (b) and upward for metal-polar, *M*-polar, phase (c).

Switching mechanisms in wurtzite ferroelectrics

The $P6_3mc$ space group of the wurtzite structure means the polarization is symmetry permitted along the crystallographic c-axis. Figure 1 shows the two allowed polarization states, as well as a hypothetical prototype phase with space group $P6_3/mmc$, which has zero polarization. In a perfect crystal, the two allowed polar states have identical energies, and are separated by a potential barrier (**Figure 2**a). In the case of ZnO, the barrier for ferroelectric switching has been estimated to be 0.25 eV/formula unit.[17,18] Among the open questions in the field are the manner in which composition changes by alloying, point defects, line defects, and area defects modify the potential profile to facilitate switching.

The historic difficulty in fully switching materials with the wurtzite structure is not surprising. As a rule of thumb, the larger the atomic displacement required to switch between two configurations, the higher the potential barrier and, consequently, the larger the coercive field. However, this heuristic does not capture the full picture, as the potential barrier also depends on factors such as bonding character, structural softness, and the specific switching mechanism. For instance, in ZnO at room temperature, the Zn atom must be displaced by 1.25 Å– approximately three times greater than the atomic displacements involved in polarization switching in $PbTiO_3$ and yet, the calculated switching barriers are similar (0.25 eV/f.u. for ZnO versus 0.20 eV/f.u. for $PbTiO_3$). Early work by Onodera et al. on Li-doped ZnO reported values for the switchable polarization of 0.044 μC/cm^2 at room temperature;[19] this is too small by a factor of ~1800–2000, suggesting that either a tiny fraction of the volume switched or that charge injection dominated the data. Similarly, Sawada et al. reported a polarization of ~6 μC/cm^2 in wurtzite BeO, which is also anomalously low.[20]

To assess whether ferroelectricity could be possible in wurtzites, Moriwake et al. conducted first-principles calculations for Zn and Be chalcogenides.[14] Many of the Zn and Be chalcogenides are quite ionic, such that the Born effective charges are comparable to the formal charges. They conclude that the barriers for intrinsic switching (e.g., in which the material uniformly/collectively changes polarization state, Figure 2a) are lower when the material is more ionic in character. The role of bond ionicity, in addition to anion-to-cation radius ratio[17] and bond stiffness,[15,21,22] in affecting the switching barriers has been recognized in subsequent works, and discussed in more detail in Reference 23. In the case of ZnO, the 0.25 eV/f.u. barrier is not that much higher than the 0.2 eV/f.u. barrier for intrinsic switching of $PbTiO_3$. In the case of ZnO, the corresponding intrinsic coercive field is 7.2 MV/cm. The models also predict that the intrinsic switching barrier should drop in cases where a c-axis oriented film is subjected to tensile stress.[14] This acts to flatten the tetrahedra by splaying the legs, and so reducing the distance that the atoms must

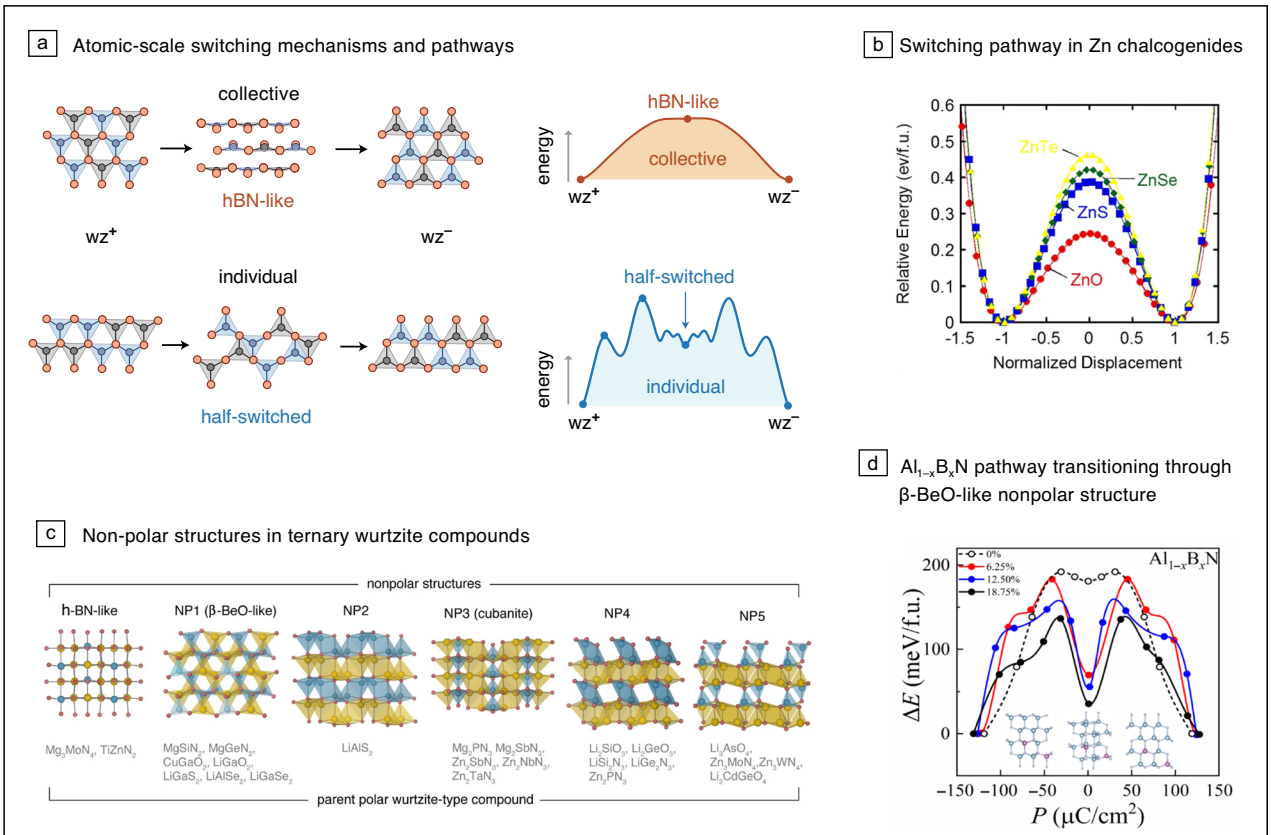

Figure 2. (a) Collective switching is characterized by a simple minimum energy pathway. Individual switching pathways involve multiple barriers and proceeds via half-switched, non-polar structures. (b) Calculated potential energy surface of Zn chalcogenides relative to cation displacement. Reprinted with permission from Reference 14. © 2014 AIP Publishing. (d) Non-polar structures identified among multinary wurtzite compounds. Reprinted with permission from Reference 15. © 2024 AAAS. (d) Calculated switching pathway for $Al_{1-x}B_xN$ alloy, where the nonpolar β-BeO-like structure is metastable. Reprinted with permission from Reference 16. © 2023 AIP Publishing.

displace for polarization reversal to occur. In practice however, intrinsic switching is rarely observed and the potential energy pathway, calculated with the solid-state nudged elastic band (SS-NEB) method, exhibits multiple barriers between the polar states, discussed next.

While the atomic-scale switching process involves phase transition(s) between polar and nonpolar states, the observation of *P*–*E* hysteresis is a result of mesoscopic switching that is understood to occur over longer length scales. Such mesoscopic switching requires the formation and motion of domains with distinct polarities. Polarization switching is inherently multiscale. The limited computational and experimental data that exist for wurtzite ferroelectrics point to significant differences in both the atomic- and domain-scale polarization switching compared to classic octahedrally bonded perovskite ferroelectrics. For example, recent computational studies have identified the structural disorder and chemical complexity as key factors enabling sequential switching of individual cation tetrahedra at the atomic scale[15] and the abrupt macroscale switching observed in $Al_{1-x}Sc_xN$ and $Al_{1-x}B_xN$ alloys requires extension of the classic Kolmogorov–Avrami–Ishibashi (KAI) model.[24] As such, a mechanistic understanding of this multiscale process is necessary to design wurtzite ferroelectrics and remediate challenges such as high coercive fields and low endurance.

As discussed in the previous section, the hBN-like structure is widely accepted as an appropriate nonpolar structure for calculating P_s of wurtzite structures, including wurtzite-type alloys such as $Al_{1-x}Sc_xN$, $Al_{1-x}B_xN$, $Al_{1-x}Gd_xN$, $Zn_{1-x}Mg_xO$, $Ga_{1-x}Sc_xN$. However, the actual switching process may not involve a phase transition wherein the structure collectively transforms through a hBN-like structure. In other words, the hBN-like structure is an appropriate choice strictly for the purposes of calculating P_s. The choice of the nonpolar structure for calculating P_s is not unique, as shown in recent studies that found half-switched, nonpolar structures and the same magnitude of P_s whether the hBN-like or the half-switched structures are used as reference non-polar structures.[15,16] The appropriate reference nonpolar structures depend on the number of unit cells considered in simulations.

Computational and experimental studies have revealed the complex nature of the atomic-scale switching mechanisms in wurtzite ferroelectrics. Early computational works by Moriwake et al.[14] (Figure 2b) and Dreyer et al.[6] used symmetry analysis

to determine the intermediate non-polar structures along the switching pathway between the positive (wz^+) and negative (wz^-) polar wurtzite structures of binary compounds, including ZnO, AlN, GaN, and InN. A collective (sometimes referred to as homogeneous) switching pathway going through the hBN-like intermediate, non-polar structure was proposed (Figure 2a). More recent computational studies have used the NEB or SS-NEB method to deduce the minimum energy pathways between wz^+ and wz^- and found the same collective mechanism ($wz^+ \rightarrow$ hBN-like $\rightarrow wz^-$) for undefective AlN and ZnO.[15,16,22] This collective mechanism is characterized by a single potential barrier where the non-polar structure is the transition state (Figure 2a).

Lee et al. showed that increased chemical complexity of compounds associated with ternary and higher stoichiometries in wurtzite-derived structures (determined by group-subgroup symmetry relations[1]) favors switching pathways with multiple potential barriers and intermediate metastable states that are transient during the switching process.[15,22] Unlike the collective mechanism, the "individual" (or sequential) cation tetrahedron undergo sequential switching in a cascading fashion; the non-polar structures are often "half-switched" (i.e., one half of the tetrahedra are one polarity and the other half of opposite polarity [Figure 2a]). Lee et al. identified five unique half-switched, nonpolar structures (Figure 2c), including the β-BeO-like structure that has been proposed in a few computational studies[15,16] and imaged using scanning transmission electron microscopy (STEM) in $Al_{1-x}B_xN$.[27]

Alloying also increases chemical complexity, in addition to introducing site disorder. The combined effect of compositional complexity and disorder lends itself to interesting switching mechanisms in wurtzite alloys. Liu et al. used the NEB method to calculate the minimum energy pathways for $Al_{1-x}B_xN$ and found that at $x > 0.0625$, the β-BeO-like non-polar structure is metastable (Figure 2d).[16] Calderon et al. confirmed the same non-polar structure in $Al_{1-x}B_xN$ with STEM.[27] By combining STEM and theoretical calculations, Mi and co-workers proposed a charged domain wall with a buckled two-dimensional hexagonal phase in $Ga_{1-x}Sc_xN$ characterized by 4–8 rings reminiscent of the β-BeO-like nonpolar structure.[28] There is now growing evidence that AlN-based alloys exhibit a composition-dependent switching mechanism. Using the SS-NEB method, Lee et al. computationally demonstrated that $Al_{1-x}Sc_xN$ alloys at low Sc compositions ($x \lesssim 0.25$–0.28) exhibit collective switching passing through a hBN-like nonpolar structure, but at higher Sc compositions gradually transitions to individual switching that passes through half-switched, nonpolar structures (**Figure 3**a). Such collective switching is still expected to occur on the scale of a few to many unit cells, but not throughout the thickness of the film. The Sc composition (x) around which the transition from collective to individual switching is observed in simulations also correspond to the compositions with onset of experimentally observed ferroelectricity in $Al_{1-x}Sc_xN$, which provides indirect validation of the computational model. Additionally, the switching barrier decreases almost linearly with x (Figure 3a), consistent with the linear decrease in coercive field observed experimentally.[8] Similar transition behavior and correspondence with thin-film compositions at which ferroelectricity is observed at or near room temperature has been reported for $Al_{1-x}B_xN$ and $Al_{1-x}Gd_xN$.[29] It must be noted that the specific compositions at which the transition in mechanism is observed are not "critical" compositions. Since the experimental realization of ferroelectricity relies on the coercive to breakdown field ratio, these specific composition ranges simply represent when the coercive fields are sufficiently larger than the breakdown fields to observe ferroelectricity at room temperature. Similar conclusions have been presented for $Zn_{1-x}Mg_xO$ in a somewhat related way. Baksa et al. showed that higher Mg substitutions induce larger local distortions and therefore, strain fluctuations that promote a change in the switching mechanism and lowering of the coercive field (Figure 3b).[25] In another study, reactive force fields were trained on density functional theory (DFT) data and used to perform molecular dynamics simulations that showed the coercive field decreases with increasing Mg substitution in $Zn_{1-x}Mg_xO$.[30]

Domain nucleation and motion in wurtzite ferroelectrics are central to understanding their polarization switching. Unlike conventional ferroelectrics, wurtzite materials exhibit unique anisotropic switching and possibly complex domain dynamics that challenge traditional theoretical models. Mesoscopic simulations are crucial for capturing these domain-scale switching mechanisms, as they bridge the gap between atomistic interactions and macroscopic behavior. Work by Andrew Rappe and co-workers has leveraged machine-learned interatomic potentials to perform large-scale simulations, providing insights into the polarization reversal process in AlN (Figure 3c).[26]

Experimental verification of ferroelectric switching pathways remains inherently challenging due to the ultrafast nature of the switching process, the high electric fields required, and the necessity for atomic-scale resolution to capture ionic displacements during the event. This demands experimental techniques capable of performing time-resolved, *in situ* biasing experiments at atomic resolution—such as transmission electron microscopy (TEM). However, accurately determining the position of every atomic species within the structure is nontrivial, requiring advanced TEM techniques and extremely thin, electron-transparent samples.

High-resolution STEM, particularly when using aberration-corrected instruments, is commonly employed. The high-angle annular dark-field (HAADF) imaging mode is widely used due to its sensitivity to atomic number (Z-contrast), but it provides limited information about light elements such as oxygen and nitrogen. To overcome this limitation, annular bright-field (ABF) and phase contrast techniques such as differential phase contrast (DPC) and center of mass (CoM) imaging have emerged, enabling simultaneous visualization of both light and heavy elements. However, it is important to note that conventional TEM provides a two-dimensional projection of the structure along

the beam direction, effectively averaging the structure over the sample thickness. This projection effect complicates the interpretation of transient or spatially varying features, such as those present during polarization switching. For instance, conventional STEM techniques may result in ambiguous interpretations of the domain walls structure in $Al_{1-x}B_xN$ and $Al_{1-x}Sc_xN$,[31] hindering the distinction between an inclined domain wall or the presence of a non-polar, β-BeO-like phase, predicted by NEB calculations.[15,16] One promising approach to addressing some of these limitations is electron ptychography, which has the potential to recover structural information as a function of sample thickness.[32] However, its application to dynamic switching processes remains an open challenge.

Defects in wurtzites and their role in ferroelectric switching

While substitutional point defects are critical to the switching energetics and can engender ferroelectricity, they and other point defects can have deleterious effects on the dielectric and ferroelectric properties, as in oxide perovskites[33] and hafnia.[34] However, the defect chemistry of wurtzite alloys and its effect on the ferroelectric behavior remain unclear. We know from fundamental physics that defects—from atomic-scale point defects to extended defects (stacking faults, dislocations, interfaces)—are likely to affect ferroelectric properties as well as dielectric breakdown.[35,36] Deep defects that introduce midgap states localize electronic carriers and minimize the leakage current but may also lead to premature defect-mediated dielectric breakdown. Shallow defects, on the other hand, contribute to increased leakage currents but may not reduce dielectric breakdown fields as strongly as deep defects. These tradeoffs are well-known qualitative concepts but quantifying these effects in wurtzite ferroelectrics is critical for future developments. Point defects are well known to modify locally the polarization switching and domain-wall motion in perovskite oxide ferroelectrics.[37] By extension, similar effects are expected in wurtzite ferroelectrics although the actual mechanisms may differ. While our discussion here focuses mainly on point defects, the importance of extended defects in III-nitrides is also widely reported.[38]

Our current understanding of the defect chemistry of wurtzite alloys is mostly based on binary wurtzite compounds, AlN, GaN, and ZnO. AlN and GaN are direct bandgap materials, with AlN classified as ultrawide bandgap (~6.2 eV) and GaN as wide bandgap (~3.4 eV).[39,40] The substantial difference in their bandgaps influences the nature and energy levels of native defects and impurities (**Figure 4**).

Native Defects: First-principles point defect calculations provide useful guidance in identifying the dominant

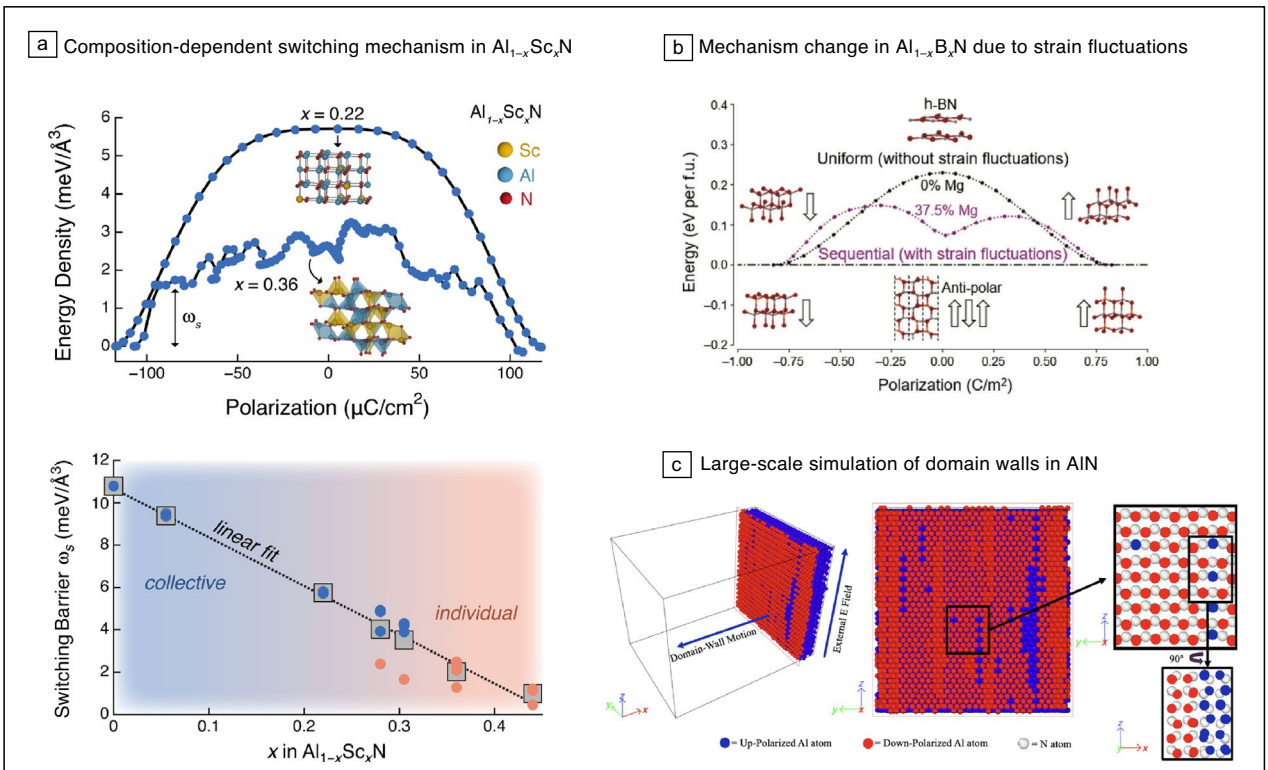

Figure 3. (a) Calculated switching pathways in $Al_{1-x}Sc_xN$ alloys at two different compositions, x. The switching mechanism changes from collective at lower Sc composition (x = 0.22) to individual at higher Sc compositions (x = 0.36). Predicted switching barrier (ω_S) changes almost linearly with x. Reprinted with permission from Reference 15. © 2024 AAAS. (b) Similar uniform to sequential mechanism change observed in $Zn_{1-x}Mg_xO$ is attributed to local strain fluctuations. Reprinted with permission from Reference 25. © 2025 Wiley. (c) Large-scale simulation of switching in AlN using machine-learned interatomic potentials show rapid switching along the wurtzite c-axis. Reprinted with permission from Reference 26.

defects and their energy levels in the bandgap. We will follow the modified Kröger–Vink notation to represent defects, A_B^C, where A is the defect (V for vacancy), B is the defect site (i for interstitial), and C is the charge state q, denoted by $q+$ or $q-$ instead of $q^{\cdot}$ and q'. The formation energy of charged defects vary with the position of the Fermi energy, E_F, which intimately depends on the growth conditions. In native AlN and GaN, cation (V_{Al}^{3-}, V_{Ga}^{3-}) and nitrogen (V_N^{1+}) vacancies are the dominant defects under both metal-rich (Al-rich or Ga-rich) and N-rich conditions (Figure 4b and c).[41–43] Under Al-rich growth conditions, nitrogen vacancies have relatively low formation energies in both AlN and GaN. However, the defect states are deeper in AlN compared to GaN, which is a consequence of the larger bandgap of AlN. For example, V_N +3/+1 and +1/0 defect states in AlN reside ~5.1 eV and ~1.5 eV below the conduction-band minimum (CBM) while in GaN the same states are at ~3.0 eV and ~0.2 eV, respectively (Figure 4a).[44,45] Experimentally, a 5.9-eV photoluminescence band in ion-implanted AlN has been attributed to a band-to-defect transition involving V_N^{1+}, where the defect state is estimated to lie approximately 0.3 eV below CBM.[46] The equilibrium Fermi energy ($E_{F,eq}$) in undoped AlN is around 2.9 eV and 1.8 eV below CBM under N-rich and Al-rich growth conditions, respectively, consistent with its highly insulating nature. The high formation energy of the dominant defects V_{Al}^{3-} and V_N^{1+} at $E_{F,eq}$, for example, >3 eV under Al-rich growth conditions, ensures very low defect concentrations. However, in practice, unintentional dopants (impurities) such as oxygen and silicon and complexes such as V_{Al} - 2(O_N) dictate the phase equilibria in AlN (Figure 4b).[44] The effect of impurities is discussed later in this section.

Unlike AlN, the only dominant defect in native GaN is V_N^{1+} (Figure 4c) under Ga-rich growth conditions. As such, V_N^{1+} are not charge compensated by V_{Al}^{3-}. Here, V_N^{1+} introduces donor defect states ~2.9 eV and ~0.25 eV below CBM. The observed n-type conductivity of GaN[47] was initially attributed to the presence of V_N, partly due to the limited accuracy of DFT functionals such as local density approximation (LDA) and generalized gradient approximation (GGA).[48,49] While V_N is a relatively shallow donor (compared to V_N in AlN), higher accuracy DFT calculations later clarified that V_N concentrations are too low to be responsible for n-type conductivity. Instead, unintentional incorporation of impurities such as oxygen and silicon is found to be the source of n-type conductivity in GaN. Cation interstitials (e.g., Ga_i) as well as antisite defects (e.g., Ga_N) are generally unfavorable in III-nitrides (Figure 4c). Recent first-principles calculations of the defect energetics in AlN-based alloys show qualitatively similar behavior to the parent III-nitrides. For example, V_N^{1+}, V_{Al}^{3-}, and V_{Sc}^{3-} are the dominant defects in native $Al_{1-x}Sc_xN$ and oxygen is a readily soluble impurity that forms deep-level DX centers.[50]

The bandgap of wurtzite ZnO (3.4 eV) is similar to GaN. Under Zn-rich/O-poor growth conditions, oxygen (V_O) and zinc vacancies (V_{Zn}) are the dominant defects, followed by zinc interstitials (Zn_i).[51,52] Under O-rich growth conditions, the neutral split oxygen interstitial (O_i) also becomes a dominant defect, in addition to V_O and V_{Zn}. The V_O (+2/0) defect level has been debated in computational studies because of the sensitivity to the DFT method.[51,53,54] Early models attributed the ubiquitous n-type conductivity of ZnO to the donor oxygen vacancies (V_O^{2+}), presumed to act as shallow donors. However, hybrid DFT calculations showed that V_O in ZnO introduces a deep donor level approximately 1.2 eV below CBM with relatively high formation energy to explain the n-type conductivity.[55,56] Thus, V_O is unlikely to contribute significantly to room-temperature free carriers. Zinc interstitials (Zn_i), by contrast, are shallow donors, but they exhibit high formation energies (>2 eV under O-poor conditions), rendering their equilibrium concentrations low. V_{Zn} introduce deep acceptors states (0/–1 and –1/–2), but their concentrations are low regardless of the growth conditions.[55,56]

Impurities: In 1973, Slack posited that oxygen incorporation in AlN occurs via substitution on the nitrogen sublattice, with charge compensation provided by Al vacancies (i.e., one Al vacancy for every three O atoms substituting N).[57] The increased V_{Al}^{3-} concentration contributes to contraction of the unit cell and reduction in thermal conductivity. Once the oxygen level exceeds a critical threshold (0.75 at.%), a new defect species emerges, wherein an Al atom adopts an octahedral coordination with O atoms. The formation of this defect mitigates the Al vacancies favored at lower O concentrations, thereby restoring the lattice parameter. Additionally, such octahedrally coordinated Al centers can serve as nucleation sites for extended O-rich defects (e.g., inversion domain boundaries [IDBs] and stacking faults).[58,59] Donor O_N^{1+} introduces an energy level approximately 0.6 eV below the conduction band. Upon capture of two electrons, O_N^{1+} undergoes structural relaxation that forms a DX center, O_N^{1+} transitioning into a deeper DX center, giving rise to an absorption band peaked at 2.22 eV.[60] Substitutional oxygen donors likely form deep-level defect complexes with V_{Al}^{3-}, resulting in acceptor levels that lie deeper in the bandgap. The $(V_{Al}^{3-} - O_N^{1+})^{2-}$ and $(V_{Al}^{3-} - 2O_N^{1+})^{1-}$ complexes correspond to acceptor levels around 1.4–1.6 eV and 1.8–2.0 eV above the valence band, depending on bonding configurations (Figure 4).[61–65] Additionally, $(V_{Al}^{3-} - O_N^{1+})^{2-}$ complexes produce 2.2 eV yellow luminescence via recombination from the shallow donor state.[66] Similarly, in GaN, O substituting for N introduces a donor level, O_N^{1+}, 0.27 eV below the conduction band.[45,67,68] This donor can also capture an extra electron to form a DX center.[45]

Silicon is another unintentional impurity that can substitute for Al or Ga, acting as a donor. In AlN, the shallow Si_{Al}^{1+} donor level transitions to deeper DX states, with ionization energies

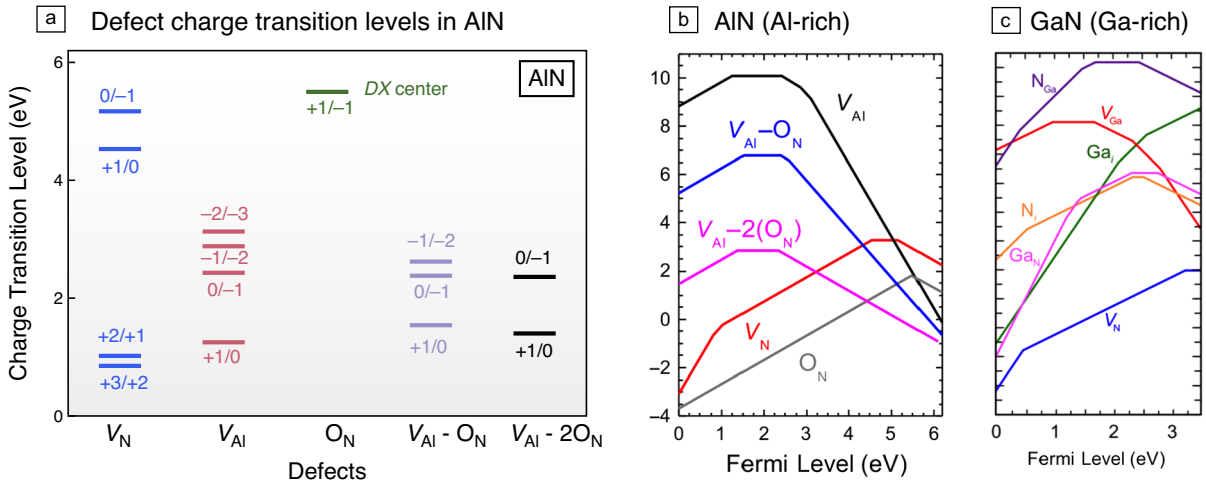

Figure 4. (a) Charge transition levels in AlN. Data from Reference 44. (b) Calculated formation energy as a function of Fermi energy of native and oxygen-related point defects in AlN under Al-rich growth conditions.[44] (c) Calculated formation energy of native defects in GaN.[45] Reprinted with permission from References 44 © 2014 AIP Publishing and 45. © 2014 Springer Nature.

ranging from 70 to 300 meV, depending on the Si concentration.[69] In GaN, Si remains a shallow donor under pressure up to 25 GPa[70] and in $Al_xGa_{1-x}N$ alloys up to $x = 0.44$.[71] Its donor level lies approximately 0.2 eV below the conduction-band minimum in GaN, thereby enhancing *n*-type conductivity.[71]

Certain growth methods, such as metal–organic chemical vapor deposition (MOCVD), can introduce high concentrations of hydrogen, which acts as an amphoteric interstitial ion in AlN and GaN. Due to the larger bandgap of AlN, the solubility of hydrogen can be substantially higher in AlN than in GaN. In *p*-type GaN, hydrogen behaves as a donor H^+, thereby compensating acceptors. Its preferred sites are the antibonding position behind a nitrogen atom or the bond-center site, where it forms a strong bond with nitrogen. The diffusion barrier for H^+ is about 0.7 eV, indicating high diffusivity at moderate to elevated temperatures. Conversely, in *n*-type GaN, hydrogen acts as an acceptor H , most stably occupying the antibonding site near a Ga atom. This configuration has a high migration barrier, leading to very low diffusivity. When the Fermi level lies below approximately 2.1 eV, H^+ is favored; for higher Fermi-level positions, H predominates.[72–74]

Extrinsic hydrogen plays a dominant role in ZnO defect chemistry, often unintentionally incorporated during crystal growth or annealing processes. Hydrogen can exist as interstitial hydrogen (H_i) or substitutional hydrogen at an oxygen site (H_O), both acting as shallow donors. The 0/+ transition level for H_i lies close to the CBM (~30 meV below), making it a highly efficient donor at room temperature.[75] Formation energy of H_i is notably lower than V_O, leading to significant incorporation even without deliberate doping. The 30-meV donor state in ZnO has also been attributed to a defect complex, Zn_i-O_N,[76] although overwhelming evidence attributes the donor state to H.

Role of alloying and defects on dielectric breakdown

In the discussion of wurtzite ferroelectrics, the changes in breakdown field (E_b) strength is often overlooked because it is generally large, but because the switching fields are very close to the E_b, it is essential that breakdown strengths are not compromised. Indeed, the key to inducing ferroelectricity in wurtzite materials is to lower E_c relative to E_b.[22] The *intrinsic* dielectric breakdown strength is intimately related to the bandgap, permittivity, and phonon properties, which all change with alloying. Typically, semiconductors with wide ($E_g > 3$ eV) and ultrawide ($E_g > 5$ eV) bandgaps, large dielectric constants ($\epsilon > 10$), and strong electron–phonon coupling (avalanche theory by von Hippel,[77] Fröhlich[78]) exhibit large intrinsic E_b. Various phenomenological models[79,80] as well as machine-learned relations[81] suggest the strong dependence of E_b on the bandgap of the material.

While alloying may flatten and lower switching barriers (Figure 3a), and by extension, reduce coercive fields, it is essential that the chemical modifications do not significantly reduce the material bandgap nor introduce appreciable concentrations of deep defects with midgap states, which facilitate carrier hopping and lower E_b. **Figure 5** compares the bandgap variations with compositions of AlN- and ZnO-based alloys. Because rocksalt ScN has a small bandgap,[85] increasing Sc composition in $Al_{1-x}Sc_xN$ causes the bandgap to shrink rapidly, reaching ~3 eV at $x > 0.3$.[82] In contrast, B alloying has an advantage in that the bandgap reduces less rapidly while the computed switching barriers are lowered sharply,[29] providing better E_b/E_c ratio. $Zn_{1-x}Mg_xO$ bandgap increases with Mg alloying, consistent with the ultrawide bandgap of rock salt MgO.

Extrinsic effects on E_b are also important, as any increases in electrical conduction can lead to thermal breakdown via Joule heating[86] or avalanche breakdown due to increased carrier hopping. The dominant defects in III-nitrides and some AlN-based alloys introduce deep defects with midgap states (Figure 4), which may be beneficial for carrier trapping that suppresses leakage currents, but facilitate carrier hopping under high electric fields leading to dielectric breakdown. Breakdown caused by the formation of conductive filaments of V_N has also been proposed,[87] although the migration barrier of V_N is known to be significantly higher than for V_O.[88]

Role of defects on film polarity, endurance, and leakage characteristics of wurtzite ferroelectrics

Oxygen and silicon impurities play a pivotal role in promoting IDBs and, thus facilitating polarity inversion in AlN films. Youngman and Harris showed that at O concentrations higher than 0.75 at.%, the formation of V_{Al}^{3-} - nO_N^{1+} defect clusters reach a threshold where aluminum coordination changes from tetrahedral to octahedral. This structural change promotes IDB formation and ultimately drives the polarity inversion.[64] Bruley et al. reported that incorporating an equivalent of 1.5 basal-plane monolayers of oxygen into the IDB is required to satisfy the Pauling charge compensation rule requirement.[89] Stolyarchuk et al. later confirmed that this same amount of oxygen enables the formation of $Al_xO_yN_z$, which is crucial for switching from N-polar to Al-polar in AlN films grown on sapphire.[90] The formation of $Al_xO_yN_z$ phase was achieved through (1) a reaction between sapphire and ammonia during nitridation; and (2) O_2 annealing or O_2 plasma treatment, which converts a mixed-polar AlN epitaxial film to Al-polar.[91,92] **Figure 6**(a)–(f) presents a high-resolution HAADF-STEM image of the AlN/sapphire interface after postannealing in N_2 at 1750°C. During annealing, Al atoms near the interface in the sapphire diffuse upward into the AlN layer, occupying V_{Al}^{3-} sites and creating an O-terminated sapphire surface, which leads to N-polar AlN formation. Simultaneously, O atoms from sapphire also diffuse into the AlN layer, forming an $Al_xO_yN_z$ layer and lead to the polarity inversion from N-polar to Al-polar.[93]

A similar process has been proposed for Si-doped AlN, where the V_{Al}^{3-} - nSi_{Al}^{1+} defect cluster is energetically favored. At low Si concentrations (<1 at.%), these clusters remain sparse and exert little impact on the wurtzite structure, preserving an Al-polar orientation. However, when Si content increases (1–15 at.%), the increasing density of V_{Al}^{3-} - nSi_{Al}^{1+} clusters promotes a transition from tetrahedral to octahedral coordination, forming IDBs and switching the film polarity from Al-polar to N-polar.[94]

Defects also found to have an effect on switching barrier for polarization reversal in $Al_{1-x}Sc_xN$ films at low Sc compositions ($x < 0.36$). Figure 6g shows the minimum energy switching pathways for both pristine AlN and defected AlN (2.8 at.% V_N^{1+} or O_N^{1+}). Introducing these defects lowers ω_s, switching barrier, relative to the pristine structure (Figure 6h).

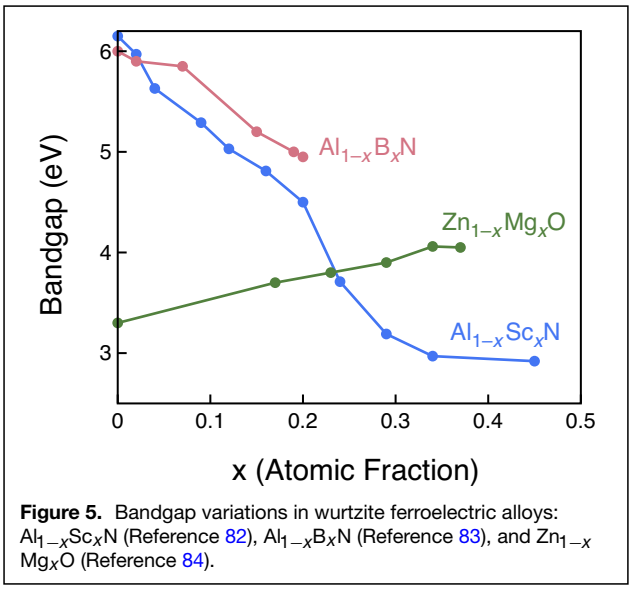

Figure 5. Bandgap variations in wurtzite ferroelectric alloys: $Al_{1-x}Sc_xN$ (Reference 82), $Al_{1-x}B_xN$ (Reference 83), and $Zn_{1-x}Mg_xO$ (Reference 84).

It was proposed that increased bond ionicity and softness reduce ω_s. Specifically, V_N^{1+} locally softens the bonds, while O_N^{1+} introduces more ionic, yet stronger, Al-O bonds. The resulting local distortions resemble those caused by Sc doping in AlN: Al-N bonds in the basal-plane shorten, and those along the *c*-axis elongate, shifting the local structure closer to the hBN-like phase.[21] In both cases, the structural changes lower ω_s.[50]

Endurance and Leakage Current Characteristics: While several wurtzite ferroelectrics are promising candidates for nonvolatile ferroelectric memories due to their high thermal stability, high remanent polarization, and CMOS compatibility, the reported endurance values 10^4–10^7 remain far below the required 10^{12} cycles.[95–97] Recently, Uehara et al. demonstrated that $Sc_xGa_{1-x}N$ exhibited no change in remanent polarization up to 1×10^8 cycles.[98] Although the intrinsic breakdown strength is approximately 15 MV/cm, the presence of defects leads to breakdown at lower electric fields, ultimately resulting in low endurance. Limited studies have explored the physical phenomena of fatigue and breakdown in wurtzite ferroelectrics under AC cycling. One study proposed that V_N exist in as-deposited $Al_{0.78}Sc_{0.22}N$ films, with additional vacancies forming during switching cycles. Prolonged cycling leads to electron trapping, which pins ferroelectric domains and reduces P_s. Newly generated V_N lower the Schottky barrier at the interface, enhancing electron tunneling and ultimately causing dielectric breakdown due to increased Joule heating (**Figure 7**a–b).[86] He et al. demonstrated that in the pristine state, the bulk conductivity of $Al_{0.93}B_{0.07}N$ is primarily governed by electron trapping at V_N sites. In the fatigued state, electron transitions between V_N^{3+} and deeper defects, such as V_{Al}^{3-} - nO_N^{1+}, become more prominent, controlling bulk conductivity (Figure 7c–d).[99]

A more recent study demonstrated that another defect level, O_N^{1+}, also contributes to increased leakage current levels in $Al_{0.65}Sc_{0.35}N$ films subjected to AC cycling. It was observed

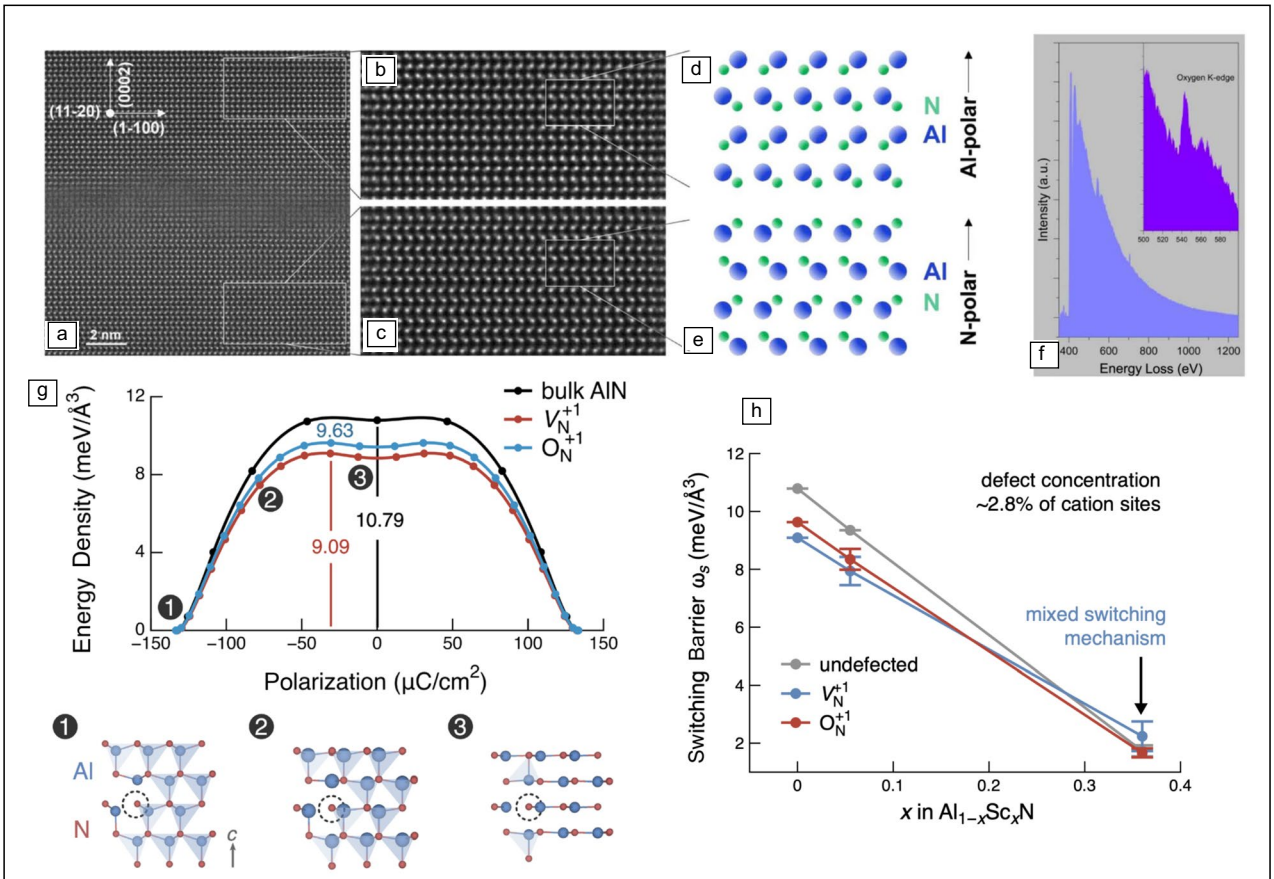

Figure 6. (a) Cross-sectional high-resolution high-angle annular dark-field-scanning transmission electron microscopy image near the HTA *c*-oriented AlN/sapphire interface. (b, c) Magnified views of the regions marked by white boxes in (a). (d, e) Schematic diagrams illustrating the atomic arrangements corresponding to (b) and (c). (f) Electron energy-loss spectroscopy spectrum at the polarity inversion interface, with the inset showing the K-edge of the O element. Reprinted with permission from Reference 93. © 2024 Royal Society Chemistry. (g) The polarization switching pathways in AlN with 2.78% V_N^{+1} and O_N^{+1} show that the presence of O_N^{+1} and V_N^{+1} reduces the switching barrier compared to defect-free AlN. Structural variations along the switching paths are depicted at points labeled "1," "2," and "3" for AlN containing 2.78% V_N^{+1}. The dashed circles highlight the positions V_N^{+1} within the structures. (h) Impact of prevalent defects on the polarization switching barrier ω_S in wurtzite $Al_{1-x}Sc_xN$ at various Sc compositions. Reprinted with permission from Reference 50. © 2024 AIP Publishing.

that oxygen migrates and penetrates through grain boundaries, leading to an increase in oxygen content from 2.3 to 12.8% after 10^7 cycles (Figure 7d). Each oxygen atom substituting for nitrogen introduces an extra electron, creating conductive channels that lead to increased leakage current, a significant reduction in remanent polarization, and eventual electrical breakdown. When the film was exposed to AC cycling in fluorinated oil, the fatigue lifetime increased significantly, along with a slower increase in leakage current (Figure 7e).[100]

The adverse effect of V_N and O_N on endurance was mitigated by postannealing the $Al_{1-x}Sc_xN$ films under NH_3 environment at 700°C, leading to improved endurance by more than two orders of magnitude (**Figure 8**a). Following NH_3 annealing, the oxygen concentration within the $Al_{1-x}Sc_xN$ film decreased from 3.5% to 2.3%, while the oxygen content at the TiN/$Al_{1-x}Sc_xN$ interface also showed a reduction. Effective removal of V_N and O_N reduced density of trapped charges, leading to lower leakage current and increased E_b (Figure 8b–c).[101] Chen et al. observed a similar increase in E_b and a reduction in leakage current when H_2 gas was introduced into the Ar/N_2 gas mixture during growth. This led to an improvement in the fatigue lifetime of $Al_{1-x}Sc_xN$ films. The effect was more pronounced in films with higher Sc content ($x = 0.26$), suggesting that a reduction in concentration of V_{Al}^{3-} - nO_N^{1+} defects may be responsible for the enhanced endurance (Figure 8d–f).[102]

Intriguingly, it was demonstrated that introducing O into bulk $Al_{0.73}Sc_{0.27}N$ through an external gas source during the reactive sputter process suppressed the leakage current by fourfold near the coercive field. In this study, the O concentration was high enough to form extended defects where Al is octahedrally bonded to oxygen. These defects act as structural units for forming IDBs, which facilitate polarization reversal. The authors demonstrated gradual transition from N- to *M*-polar orientation as the oxygen content in the film increased.[103]

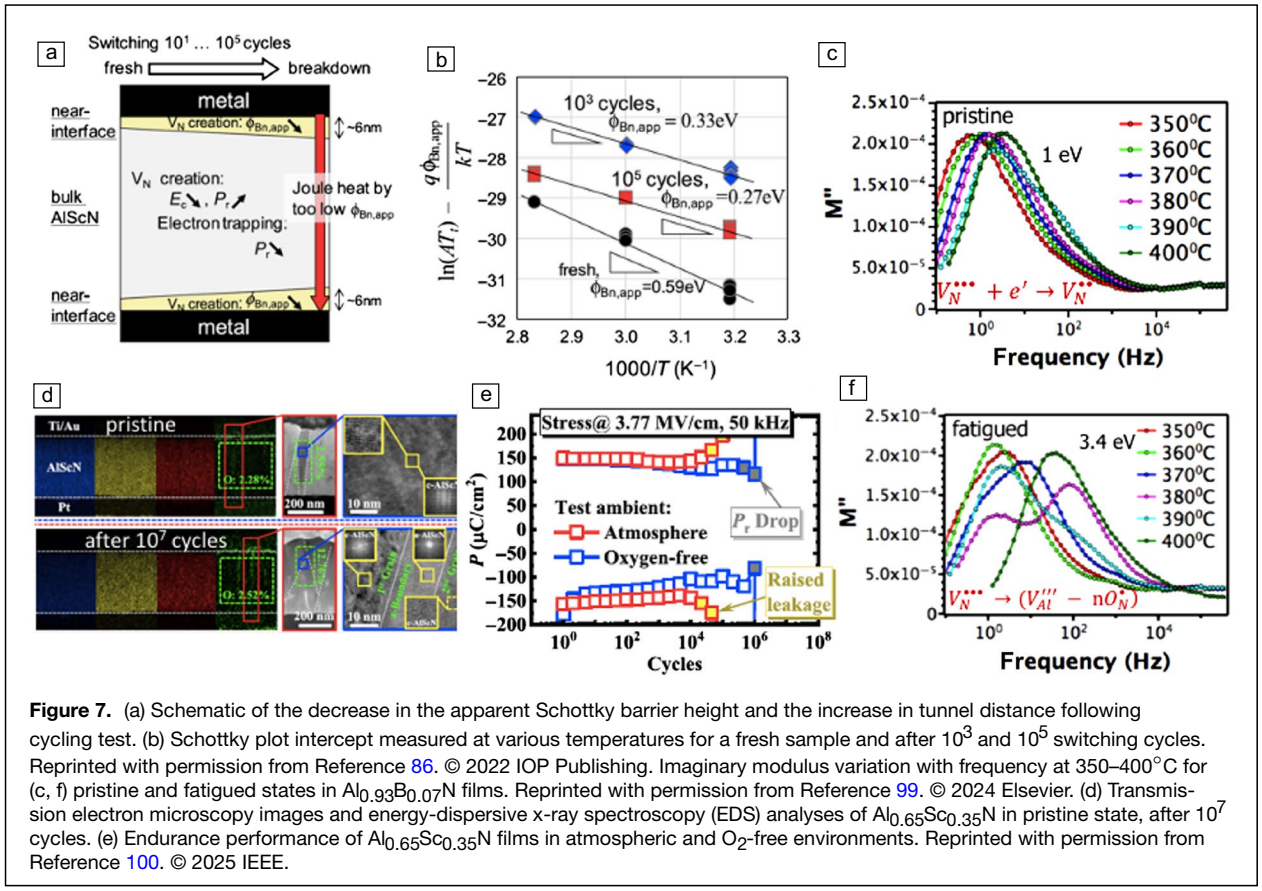

Figure 7. (a) Schematic of the decrease in the apparent Schottky barrier height and the increase in tunnel distance following cycling test. (b) Schottky plot intercept measured at various temperatures for a fresh sample and after 10^3 and 10^5 switching cycles. Reprinted with permission from Reference 86. © 2022 IOP Publishing. Imaginary modulus variation with frequency at 350–400°C for (c, f) pristine and fatigued states in $Al_{0.93}B_{0.07}N$ films. Reprinted with permission from Reference 99. © 2024 Elsevier. (d) Transmission electron microscopy images and energy-dispersive x-ray spectroscopy (EDS) analyses of $Al_{0.65}Sc_{0.35}N$ in pristine state, after 10^7 cycles. (e) Endurance performance of $Al_{0.65}Sc_{0.35}N$ films in atmospheric and O_2-free environments. Reprinted with permission from Reference 100. © 2025 IEEE.

Outlook

The recent discovery and rapid development of wurtzite ferroelectrics opens numerous possibilities for their use in an array of electronic and electro-optical devices. Over the past five years, experimental and computational studies have provided fundamental insight into switching mechanisms and pathways in these alloyed materials. Less, however, is known about the mechanisms of domain movement and their dynamics, necessitating ongoing investigation.

The relative simplicity of the wurtzite structure, chemical simplicity of many ferroelectric compositions, and low-temperature synthesis conditions also facilitate scaling to large wafer sizes at back-end-of-line (BEOL)-compatible temperatures. In particular, these materials offer a potential avenue to achieve high density non-volatile memory. Among the key factors that will need to be overcome to move these materials forward in this application space are adequate reliability over the lifetime of the memory element. Improved reliability demands better understanding and control of deleterious point defects. In parallel, there is also a need to further reduce the coercive field to reduce carrier injection during the switching process. Reduced coercive fields will also facilitate their use in ferroelectric field-effect transistors (FeFETs). Beyond their interest in memory applications, the large electro-optic coefficients of the wurtzite materials also provide the tantalizing prospect of nonlinear optical components, which could be integrated on semiconductors without the need for wafer bonding (as is currently required for lithium niobate and lithium tantalate). For this latter application, the ability to create controlled (and potentially rewriteable) polarization patterns is appealing for second-harmonic generation. Here, it may be necessary to develop new approaches to induce local polarization reversal without electrodes, to minimize optical losses. Likewise, reduction of midgap defect states to reduce the propensity for absorption at the use wavelengths will also be required.

While ongoing research is needed to better understand domain dynamics and to control point defects in this new class of ferroelectrics, the field continues to rapidly advance. Since (Al, Sc)N is already widely adopted in piezoelectric resonators for acoustic filters in cellular communications, a preexisting industrial base for materials deposition and patterning exists, which may accelerate adoption into these new application spaces.

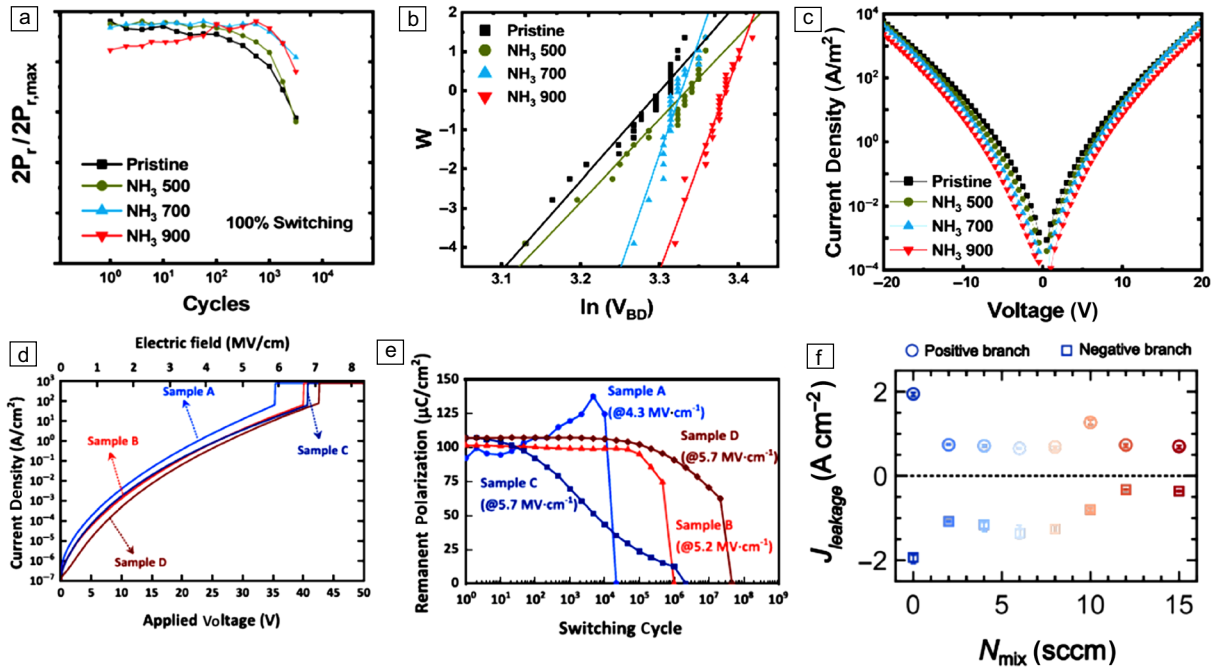

Figure 8. (a) Fatigue behavior, (b) Weibull distribution of breakdown voltage, (c) leakage current characteristics of Al, ScN films in their pristine state and after annealing under NH_3 at 500°C, 700°C, and 900°C. Reprinted with permission from Reference 101. © 2023 Royal Society of Chemistry. (d) Variation in leakage current density, (e) endurance characteristics for the sputtered films with different Al/Sc ratios and input gas: Sample A: $Al_{0.53}Sc_{0.47}N$ in Ar/N_2, Sample B: $Al_{0.53}Sc_{0.47}N$ in $Ar/N_2/3\%H_2$, Sample C: $Al_{0.80}Sc_{0.20}N$ in Ar/N_2, and Sample D: $Al_{0.80}Sc_{0.20}N$ in $Ar/N_2/3\%$ H_2. Reprinted with permission from Reference 102. © 2024 IOP Publishing. (f) Leakage current density of $Al_{0.73}Sc_{0.27}N$ kHz, measured at 5.2 MV/cm (near E_c) at 5 kHz. The films were grown using distinct N_2:O_2 gas flow ratios, with N_{mix} = 0, 8, and 15 sccm. Reprinted with permission from Reference 103. © 2025 Wiley.

Author contributions

H.M.: Conceptualization, writing–original draft and review and editing. B.A.A.: Conceptualization, resources, writing–original draft and review and editing, funding. S.C.: Writing–original draft and review and editing. E.C.D.: Conceptualization, resources, writing–original draft and review and editing, supervision, funding. P.G.: Conceptualization, resources, writing–original draft and review and editing, supervision, funding.

Funding

Open Access funding provided by Carnegie Mellon University. P.G. and E.C.D acknowledge support from the National Science Foundation under Grant No. DMR-2119281. B.A.A., S.C., and E.C.D gratefully acknowledge support from the US Department of Energy, Office of Science, Office of Basic Energy Sciences, Energy Frontier Research Centers program under Award No. DE-SC0021118. H.M. was supported by the MEXT Program: Data Creation and Utilization Type Material Research and Development Project Grant No. JPMXP1122683430, and JSPS KAKENHI Grant-in-Aid for Scientific Research (B) Grant No. JP23H01689.

Conflict of interest

The authors declare no conflict of interest.

Open Access

This article is licensed under a Creative Commons Attribution 4.0 International License, which permits use, sharing, adaptation, distribution and reproduction in any medium or format, as long as you give appropriate credit to the original author(s) and the source, provide a link to the Creative Commons licence, and indicate if changes were made. The images or other third party material in this article are included in the article's Creative Commons licence, unless indicated otherwise in a credit line to the material. If material is not included in the article's Creative Commons licence and your intended use is not permitted by statutory regulation or exceeds the permitted use, you will need to obtain permission directly from the copyright holder. To view a copy of this licence, visit http://creativecommons.org/licenses/by/4.0/.

References

1. J. Breternitz, S. Schorr, *Acta Crystallogr.* **A77**, 1 (2021)
2. O. Ambacher, B. Foutz, J. Smart, J. Shealy, N. Weimann, K. Chu, M. Murphy, A. Sierakowski, W. Schaff, L. Eastman, R. Dimitrov, A. Mitchell, M. Stutzmann, *J. Appl. Phys.* **87**, 334 (2000)
3. R.D. King-Smith, D. Vanderbilt, *Phys. Rev. B* **47**, 1651 (1993)
4. R. Resta, *Rev. Mod. Phys.* **66**, 899 (1994)
5. N.A. Spaldin, *J. Solid State Chem.* **195**, 2 (2012)
6. C.E. Dreyer, A. Janotti, C.G. Walle, D. Vanderbilt, *Phys. Rev. X* **6**, 021038 (2016)
7. F. Bernardini, V. Fiorentini, D. Vanderbilt, *Phys. Rev. B* **56**, 10024 (1997)

8. S. Fichtner, N. Wolff, F. Lofink, L. Kienle, B. Wagner, *J. Appl. Phys.* **125**, 114103 (2019)
9. X.N. Zhu, X. Chen, H. Tian, X.M. Chen, *RSC Adv.* **7**, 22587 (2017)
10. Y. Sun, A.Y. Abid, C. Tan, C. Ren, M. Li, N. Li, P. Chen, Y. Li, J. Zhang, X. Zhong, J Wang, M. Liao, K. Liu, X. Bai, Y. Zhou, D. Yu, P. Gao, *Sci. Adv.* **5**, 4355 (2019)
11. X. Wu, D. Vanderbilt, D.R. Hamann, *Phys. Rev. B* **72**, 035105 (2005)
12. V.S. Calderon, J. Hayden, M. Delower, J.-P. Maria, E.C. Dickey, *APL Mater.* **12**, 021105 (2024)
13. S. Calderon, S.D. Funni, E.C. Dickey, *Microsc. Microanal.* **28**, 2047 (2022)
14. H. Moriwake, A. Konishi, T. Ogawa, K. Fujimura, C.A.J. Fisher, A. Kuwabara, T. Shimizu, S. Yasui, M. Itoh, *Appl. Phys. Lett.* **104**, 242909 (2014)
15. C.-W. Lee, K. Yazawa, A. Zakutayev, G.L. Brennecka, P. Gorai, *Sci. Adv.* **10**, 0848 (2024)
16. Z. Liu, X. Wang, X. Ma, Y. Yang, D. Wu, *Appl. Phys. Lett.* **122**, 122901 (2023)
17. H. Moriwake, R. Yokoi, A. Taguchi, T. Ogawa, C.A.J. Fisher, A. Kuwabara, Y. Sato, T. Shimizu, Y. Hamasaki, H. Takashima, M. Itoh, *APL Mater.* **8**, 121102 (2020)
18. A. Konishi, T. Ogawa, C.A.J. Fisher, A. Kuwabara, T. Shimizu, S. Yasui, M. Itoh, H. Moriwake, *Appl. Phys. Lett.* **109**, 102903 (2016)
19. A. Onodera, *Ferroelectrics* **267**(1), 131 (2002). https://doi.org/10.1080/00150190210997
20. S. Sawada, S. Hirotsu, H. Iwamura, Y. Shiroishi, *J. Phys. Soc. Jpn.* **35**, 946 (1973)
21. K. Yazawa, J.S. Mangum, P. Gorai, G.L. Brennecka, A. Zakutayev, *J. Mater. Chem. C* **10**, 17557 (2022)
22. C.-W. Lee, N.U. Din, K. Yazawa, G.L. Brennecka, A. Zakutayev, P. Gorai, *Matter* **7**, 1644 (2024)
23. S. Fichtner, G. Schönweger, C.-W. Lee, K. Yazawa, P. Gorai, G.L. Brennecka, *Appl. Phys. Rev.* **12**, 021310 (2025)
24. K. Yazawa, J. Hayden, J.-P. Maria, W. Zhu, S. Trolier-McKinstry, A. Zakutayev, G.L. Brennecka, *Mater. Horiz.* **10**, 2936 (2023)
25. S.M. Baksa, S. Gelin, S. Oturak, R.J. Spurling, A. Sepehrinezhad, L. Jacques, S.E. Trolier-McKinstry, A.C.T. Duin, J.-P. Maria, A.M. Rappe, I. Dabo, *Adv. Electron. Mater.* **11**, 2400567 (2025)
26. D. Behrendt, A. Samanta, A.M. Rappe, Ferroelectric fractals: Switching mechanism of wurtzite AlN (2024), Preprint, https://arxiv.org/abs/2410.18816
27. S. Calderon, J. Hayden, S.M. Baksa, W. Tzou, S. Trolier-McKinstry, I. Dabo, J.-P. Maria, E.C. Dickey, *Science* **380**, 1034 (2023)
28. D. Wang, D. Wang, M. Molla, Y. Liu, S. Yang, S. Yuan, J. Liu, M. Hu, Y. Wu, T. Ma, K. Sun, H. Guo, E. Kioupskis, Z. Mi, *Nature* **641**, 76 (2025)
29. C.-W. Lee, R.W. Smaha, G.L. Brennecka, N.M. Haegel, P. Gorai, K. Yazawa, *APL Mater.* **13**, 021114 (2025)
30. A. Sepehrinezhad, S.M. Baksa, I. Dabo, A.C. Duin, *J. Phys. Chem. C* **128**, 12534 (2024)
31. N. Wolff, G. Schönweger, I. Streicher, M.R. Islam, N. Braun, P. Straňák, L. Kirste, M. Prescher, A. Lotnyk, H. Kohlstedt, S. Leone, L. Kienle, S. Fichtner, *Adv. Phys. Res.* **3**, 2300113 (2024)
32. Z. Chen, Y. Jiang, Y.-T. Shao, M.E. Holtz, M. Odstrčil, M. Guizar-Sicairos, I. Hanke, S. Ganschow, D.G. Schlom, D.A. Muller, *Science* **372**, 826 (2021)
33. P. Gao, C.T. Nelson, J.R. Jokisaari, S.-H. Baek, C.W. Bark, Y. Zhang, E. Wang, D.G. Schlom, C.-B. Eom, X. Pan, *Nat. Commun.* **2**, 591 (2011)
34. A. Chouprik, D. Negrov, E.Y. Tsymbal, A. Zenkevich, *Nanoscale* **13**, 11635 (2021)
35. J. Boksiner, P. Leath, *Phys. Rev. E* **57**, 3531 (1998)
36. P.P. Budenstein, *IEEE Trans. Electr. Insul.* **EI-15**, 225 (1980)
37. M. Otonicar, M. Dragomir, T. Rojac, *J. Am. Ceram. Soc.* **105**, 6479 (2022)
38. J. Speck, S. Rosner, *Physica B* **273**, 24 (1999)
39. M. Feneberg, R.A. Leute, B. Neuschl, K. Thonke, M. Bickermann, *Phys. Rev. B* **82**, 075208 (2010)
40. F. Roccaforte, P. Fiorenza, G. Greco, R.L. Nigro, F. Giannazzo, F. Iucolano, M. Saggio, *Microelectron. Eng.* **187-188**, 66 (2018)
41. C. Stampfl, C. Walle, *Phys. Rev. B* **65**, 155212 (2002)
42. Y. Zhang, W. Liu, H. Niu, *Phys. Rev. B* **77**, 035201 (2008)
43. K. Laaksonen, M.G. Ganchenkova, R.M. Nieminen, *J. Phys. Condens. Matter* **21**, 015803 (2008)
44. Q. Yan, A. Janotti, M. Scheffler, C.G. Walle, *Appl. Phys. Lett.* **105**, 111104 (2014)
45. J.L. Lyons, C.G. Walle, *NPJ Comput. Mater.* **3**, 1 (2017)
46. N. Nepal, K. Nam, M. Nakarmi, J. Lin, H. Jiang, J. Zavada, R. Wilson, *Appl. Phys. Lett.* **84**, 1090 (2004)
47. H.P. Maruska, J. Tietjen, *Appl. Phys. Lett.* **15**, 327 (1969)
48. J. Neugebauer, C.G. Walle, *Phys. Rev. B* **50**, 8067 (1994)
49. T. Mattila, R.M. Nieminen, *Phys. Rev. B* **55**, 9571 (1997)
50. C.-W. Lee, N.U. Din, G.L. Brennecka, P. Gorai, *Appl. Phys. Lett.* **125**, 022901 (2024)
51. A. Janotti, C.G. Walle, *Phys. Rev. B* **76**, 165202 (2007)
52. A. Janotti, C.G. Walle, *Rep. Prog. Phys.* **72**, 126501 (2009)
53. S. Lany, A. Zunger, *Phys. Rev. B* **72**, 035215 (2005)
54. T.R. Paudel, W.R. Lambrecht, *Phys. Rev. B* **77**, 205202 (2008)
55. S. Clark, J. Robertson, S. Lany, A. Zunger, *Phys. Rev. B* **81**, 115311 (2010)
56. F. Oba, A. Togo, I. Tanaka, J. Paier, G. Kresse, *Phys. Rev. B* **77**, 245202 (2008)
57. G.A. Slack, *J. Phys. Chem. Solids* **34**, 321 (1973)
58. J. Harris, R. Youngman, R. Teller, *J. Mater. Res.* **5**, 1763 (1990)
59. M. Denanot, J. Rabier, *J. Mater. Sci.* **24**, 1594 (1989)
60. Q. Yan, J.L. Lyons, L. Gordon, A. Janotti, C.G. Walle, *Appl. Phys. Lett.* **126**, 062106 (2025)
61. L. Gordon, J. Lyons, A. Janotti, C. Walle, *Phys. Rev. B* **89**, 085204 (2014)
62. C. Kai, H. Zang, J. Ben, K. Jiang, Z. Shi, Y. Jia, X. Cao, W. Lü, X. Sun, D. Li, *J. Lumin.* **235**, 118032 (2021)
63. A. Sedhain, J. Lin, H. Jiang, *Appl. Phys. Lett.* **100**, 221107 (2012)
64. R.A. Youngman, J.H. Harris, *J. Am. Ceram. Soc.* **73**, 3238 (1990)
65. J. Pastrňák, S. Pačesová, L. Roskovcova, *Czech. J. Phys. B* **24**, 1149 (1974)
66. T. Mattila, A.P. Seitsonen, R.M. Nieminen, *Phys. Rev. B* **54**, 1474 (1996)
67. J. Neugebauer, C.G. Walle, *Appl. Phys. Lett.* **69**, 503 (1996)
68. J. Oila, V. Ranki, J. Kivioja, K. Saarinen, P. Hautojärvi, J. Likonen, J. Baranowski, K. Pakula, T. Suski, M. Leszczynski, I. Grzegory, *Phys. Rev. B* **63**, 045205 (2001)
69. R. Vermeersch, G. Jacopin, B. Daudin, J. Pernot, *Appl. Phys. Lett.* **120**, 162104 (2022)
70. C. Wetzel, T. Suski, J. Ager Iii, E. Weber, E. Haller, S. Fischer, B.K. Meyer, R. Molnar, P. Perlin, *Phys. Rev. Lett.* **78**, 3923 (1997)
71. W. Götz, N. Johnson, C. Chen, H. Liu, C. Kuo, W. Imler, *Appl. Phys. Lett.* **68**, 3144 (1996)
72. C.G. Walle, J. Neugebauer, *J. Appl. Phys.* **95**, 3851 (2004)
73. J. Li, J. Lin, H. Jiang, A. Salvador, A. Botchkarev, H. Morkoc, *Appl. Phys. Lett.* **69**, 1474 (1996)
74. C.G. Walle, *Phys. Rev. B* **56**, 10020 (1997)
75. C.G. Walle, *Phys. Rev. Lett.* **85**, 1012 (2000)
76. D.C. Look, G.C. Farlow, P. Reunchan, S. Limpijumnong, S. Zhang, K. Nordlund, *Phys. Rev. Lett.* **95**, 225502 (2005)
77. A. von Hippel, *J. Appl. Phys.* **8**, 815 (1937)
78. H. Fröhlich, *Proc. R. Soc. Lond. A* **160**, 230 (1937)
79. J.L. Hudgins, G.S. Simin, E. Santi, M.A. Khan, *IEEE Trans. Power Electron.* **18**(3), 907 (2003)
80. S.M. Sze, G. Gibbons, *Appl. Phys. Lett.* **8**, 111 (1966)
81. C. Kim, G. Pilania, R. Ramprasad, *Chem. Mater.* **28**, 1304 (2016)
82. R. Deng, S.R. Evans, D. Gall, *Appl. Phys. Lett.* **102**, 112103 (2013)
83. J. Hayden, M.D. Hossain, Y. Xiong, K. Ferri, W. Zhu, M.V. Imperatore, N. Giebink, S. Trolier-McKinstry, I. Dabo, J.-P. Maria, *Phys. Rev. Mater.* **5**, 044412 (2021)
84. K. Ferri, S. Bachu, W. Zhu, M. Imperatore, J. Hayden, N. Alem, N. Giebink, S. Trolier-McKinstry, J.-P. Maria, *J. Appl. Phys.* **130**, 044101 (2021)
85. Z. Gu, J. Edgar, J. Pomeroy, M. Kuball, D. Coffey, *J. Mater. Sci. Mater. Electron.* **15**, 555 (2004)
86. S.-L. Tsai, T. Hoshii, H. Wakabayashi, K. Tsutsui, T.-K. Chung, E.Y. Chang, K. Kakushima, *Jpn. J. Appl. Phys.* **61**, 1005 (2022)
87. R. Guido, T. Mikolajick, U. Schroeder, P.D. Lomenzo, *Nano Lett.* **23**, 7213 (2023)
88. Q. Ren, X. Liu, Z. Ding, Y. Liu, Q. Zhou, Q. Qian, G. Zhang, H. Li, N. Wang, *ACS Appl. Mater. Interfaces* **16**, 28838 (2024)
89. J. Bruley, A. Westwood, R.A. Youngman, J.-C. Zhao, M.R. Notis, *MRS Online Proc. Libr.* **357**, 265 (1994)
90. N. Stolyarchuk, T. Markurt, A. Courville, K. March, J. Zúñiga-Pérez, P. Vennéguès, M. Albrecht, *Sci. Rep.* **8**, 14111 (2018)
91. S. Mohn, N. Stolyarchuk, T. Markurt, R. Kirste, M.P. Hoffmann, R. Collazo, A. Courville, R. Di Felice, Z. Sitar, P. Vennéguès, M. Albrecht, *Phys. Rev. Appl.* **5**, 054004 (2016)
92. N. Stolyarchuk, T. Markurt, A. Courville, K. March, O. Tottereau, P. Vennéguès, M. Albrecht, *J. Appl. Phys.* **122**, 155303 (2017)
93. K. Jiang, J. Ben, X. Sun, Z. Shi, X. Wang, T. Fang, S. Zhang, S. Lv, Y. Chen, Y. Jia, H. Zang, M. Liu, D. Li, *Nanoscale Adv.* **6**, 418 (2024)
94. S.A. Anggraini, M. Uehara, K. Hirata, H. Yamada, M. Akiyama, *Sci. Rep.* **10**, 4369 (2020)
95. D. Wang, P. Wang, S. Mondal, S. Mohanty, A.E. Tao. Ma, Z. Mi, *Adv. Electron. Mater.* **8**, 2200005 (2022)
96. T. Mikolajick, S. Slesazeck, H. Mulaosmanovic, M.H. Park, S. Fichtner, P. Lomeenzo, M. Hoffmann, U. Schroeder, *J. Appl. Phys.* **129**, 100901 (2021)
97. X. Liu, D. Wang, K.-H. Kim, K. Katti, P. Musavigharavi, J. Miao, E.A. Stach, R.H. Ollson, D. Jariwala, *Nano Lett.* **21**, 3753 (2021)
98. M. Uehara, K. Hirata, Y. Nakamura, S.A. Anggraini, K. Okamoto, H. Yamada, H. Funakubo, M. Akiyama, A*PL Mater.* **12**, 121102 (2024)
99. F. He, W. Zhu, J. Hayden, J. Casamento, Q. Tran, K. Kang, Y. Song, B. Akkopru-Akgun, J.I. Yang, P. Tipsawat, G. Brennecka, S. Choi, T.N. Jackson, J.-P. Maria, S. Trolier-McKinstry, *Acta Mater.* **266**, 119678 (2024)
100. R. Wang, J. Zhou, D. Yao, S. Zheng, B. Li, X. Li, Y. Liu, Y. Hao, G. Han, *IEEE Electron Device Lett.* **46**, 382 (2025)
101. K. Do Kim, Y.B. Lee, S.H. Lee, I.S. Lee, S.K. Ryoo, S.Y. Byun, J.H. Lee, C.S. Hwang, *Nanoscale* **15**, 16390 (2023)
102. S.-M. Chen, T. Hoshii, H. Wakabayashi, K. Tsutsui, E.Y. Chang, K. Kakushima, *Jpn. J. Appl. Phys.* **63**, 03 (2024)
103. M.R. Islam, N. Wolff, G. Schönweger, T.-N. Kreutzer, M. Brown, M. Gremmel, E.S. Ollanescu-Orendi, P. Straňák, L. Kirste, G.L. Brennecka, S. Fitchner, L. Kienle, *Adv. Electron. Mater.* **11**, 2400874 (2025) □

Publisher's note
Springer Nature remains neutral with regard to jurisdictional claims in published maps and institutional affiliations.

Hiroki Moriwake is a materials scientist specializing in computational design of electronic ceramics and battery materials, including ferroelectrics and dielectrics. He received his PhD degree from Kyoto University, Japan, in 2001. As a senior researcher at Japan Fine Ceramics Center, Japan, and a visiting professor at Tokyo University of Science, Japan, he leads an Acquisition, Technology & Logistics Agency-funded project integrating density functional theory and machine learning with experimental collaboration. His work has earned multiple awards, including the Academic Award of The Ceramic Society of Japan. Moriwake can be reached by email at moriwake@jfcc.or.jp.

Betul Akkopru-Akgun is an Assistant Research Professor in the Materials Research Institute at The Pennsylvania State University (Penn State). She holds PhD and MSc degrees in materials science and engineering from Penn State, as well as a second MSc degree in metallurgical and materials engineering from the Middle East Technical University, Turkey. Her research focuses on unraveling the correlation between defect dynamics, coercive fields, leakage currents, and endurance characteristics in ferroelectric thin films. She investigates defects, domain walls, interfaces, and intermediate switching structures across multiple length scales. Akkopru-Akgun can be reached by email at bua134@psu.edu.

Sebastian Calderon serves as a Special Faculty member at Carnegie Mellon University. He holds a PhD degree in materials engineering from the University of Minho, Portugal, with BSc and MSc degrees from the National University of Colombia. His research focuses on advancing transmission electron microscopy/scanning transmission electron microscopy imaging and spectroscopy techniques for materials characterization. He held a Marie-Curie Co-fund postdoctoral position at the International Iberian Nanotechnology Laboratory, Portugal, and at Carnegie Mellon University. His current work aims at the atomic-scale characterization of ferroelectrics to explore their dynamic behavior and applications for electronic devices. Calderon can be reached by email at scaldero@andrew.cmu.edu.

Elizabeth C. Dickey is the Teddy & Wilton Hawkins Distinguished Professor and Department Head of Materials Science and Engineering at Carnegie Mellon University. She is also a Fellow of the Materials Research Society, The American Ceramic Society, the Microscopy Society of America, and AAAS. She has ~25 years of experience in developing processing–structure–property relationships for ceramics and ceramic composites for advanced aerospace and electronic-device applications. She is regarded as a leader in the application of electron microscopy to understand the role of material defects on electrical and chemical transport and polarization in electronic ceramics. Dickey can be reached by email at ecdickey@cmu.edu.

Prashun Gorai is an Assistant Professor in Chemical and Biological Engineering at Rensselaer Polytechnic Institute and holds a joint appointment at the National Renewable Energy Laboratory. He combines quantum mechanical calculations, high-throughput computing, and machine learning to accelerate the discovery and design of materials for energy and microelectronics. His current work aims to discover novel wurtzite ferroelectric materials and uncover polarization switching mechanisms. He has received several honors, including the International Thermoelectric Society Young Investigator Award and *Chemistry of Materials* Lectureship Award. Gorai can be reached by email at goraip@rpi.edu.